inorganics

MDPI

Article

Luminescence Efficiency and Spectral Compatibility of Cerium Fluoride (CeF_3) Inorganic Scintillator with Various Optical Sensors in the Diagnostic Radiology X-ray Energy Range

Vasileios Ntoupis [1], Christos Michail [1,*], Nektarios Kalyvas [1], Athanasios Bakas [2], Ioannis Kandarakis [1], George Fountos [1] and Ioannis Valais [1]

[1] Radiation Physics, Materials Technology and Biomedical Imaging Laboratory, Department of Biomedical Engineering, University of West Attica, Ag. Spyridonos, 12210 Athens, Greece; vdoupis@uniwa.gr (V.N.); nkalyvas@uniwa.gr (N.K.); kandarakis@uniwa.gr (I.K.); gfoun@uniwa.gr (G.F.); valais@uniwa.gr (I.V.)
[2] Department of Biomedical Sciences, University of West Attica, Ag. Spyridonos, 12210 Athens, Greece; abakas@uniwa.gr
* Correspondence: cmichail@uniwa.gr

Abstract: The aim of this study was to experimentally assess the luminescence efficiency of a cerium fluoride (CeF_3) inorganic scintillator in crystal form as a possible alternative to high-luminescence but hygroscopic cerium bromide ($CeBr_3$). The experiments were performed under typical diagnostic radiology X-rays (50–140 kVp). Parameters such as the crystal's absolute luminescence efficiency (AE) and the spectral matching with a series of optical detectors were examined. The replacement of bromine with fluorine appeared to drastically reduce the AE of CeF_3 compared to $CeBr_3$ and other commercially available inorganic scintillators such as bismuth germanate ($Bi_4Ge_3O_{12}$-BGO). CeF_3 reaches a maximum luminescence efficiency value of only 0.8334 efficiency units (EUs) at 140 kVp, whereas the corresponding values for $CeBr_3$ and BGO were 29.49 and 3.41, respectively. Furthermore, the emission maximum (at around 313 nm) moved towards the lower part of the visible spectrum, making CeF_3 suitable for spectral coupling with various photocathodes and photomultipliers applied in nuclear medicine detectors, but completely unsuitable for spectral matching with CCDs and CMOS. The obtained luminescence efficiency results denote that CeF_3 cannot be applied in medical imaging applications covering the range 50–140 kVp; however, examination of its luminescence output in the nuclear medicine energy range (~70 to 511 keV) could reveal possible applicability in these modalities.

Keywords: inorganic scintillators; crystals; X-ray radiation; medical detectors; cerium fluoride; medical imaging

check for updates

Citation: Ntoupis, V.; Michail, C.; Kalyvas, N.; Bakas, A.; Kandarakis, I.; Fountos, G.; Valais, I. Luminescence Efficiency and Spectral Compatibility of Cerium Fluoride (CeF_3) Inorganic Scintillator with Various Optical Sensors in the Diagnostic Radiology X-ray Energy Range. *Inorganics* **2024**, *12*, 230. https://doi.org/10.3390/inorganics12080230

Academic Editor: Nabanita Saikia

Received: 1 July 2024
Revised: 9 August 2024
Accepted: 13 August 2024
Published: 22 August 2024

Copyright: © 2024 by the authors. Licensee MDPI, Basel, Switzerland. This article is an open access article distributed under the terms and conditions of the Creative Commons Attribution (CC BY) license (https://creativecommons.org/licenses/by/4.0/).

1. Introduction

Research on novel inorganic scintillators for a variety of applications, including medical applications, is an ongoing task for research groups worldwide [1–11]. An efficient single-crystal scintillator with a light yield of the order of 6×10^4 photons/MeV is cerium bromide ($CeBr_3$). It also has a decay time of only 19 ns [12] and a spectrum lying in the lower part of the visible range, making it suitable for coupling with various optical detectors used in nuclear medicine [13–21].

However, $CeBr_3$ is hygroscopic and should be encapsulated in order to maintain its structural integrity, leading to a reduction in the luminescence signal [22]. A material with a similar structure with the bromine (Br) atom replaced by fluorine (F) is cerium fluoride (CeF_3) [13,23–28].

CeF_3 has been in the spotlight in the last 30 years due to experiments including the Large Hadron Collider (LHC) [29–38]. Since CeF_3 single crystals have attractive optical, mechanical and luminescence characteristics, they are suitable for a variety of applications [25,29,39–42]. CeF_3 crystals are rare-earth trifluorides with a tysonite structure [43].

The crystalline structure can be hexagonal, as per the crystal sample used in our study, at high temperatures and trigonal at low ones [43]. CeF_3's hexagonal-shape crystalline structure includes layers of cerium ions situated very close together. At the same time, fluorine ions occupy three distinct positions inside the lattice [43–45]. Previous X-ray diffraction (XRD) analysis exhibits characteristic peaks that agree with the hexagonal structure of the crystal [43–45]. Optical and structural properties, such as a large Verdet constant (247 rad/Tm at 450 nm), high transmittance of the crystal, about 92% compared to terbium gallium garnet (TGG) and a great cutoff absorption edge (at 270 nm compared to 400 nm for the TGG crystal), render it a good scintillator candidate for magneto-optical materials and mostly for various optical applications in the region of high-energy physics [46,47].

Furthermore, a CeF_3 crystal's mechanical properties reveal an important anisotropy. Young's modulus anisotropy (E_{max}/E_{min} = 195 GPa/100 GPa = 1.95), shear modulus anisotropy (G_{max}/G_{min} = 65.7 GPa/34.2 GPa = 1.92), Poisson's ratio (0.16–0.48) and Vickers microhardness (2.3–2.9 GPa) make CeF_3 crystals very useful for technologies that need flexible and durable materials [45].

It has been discovered in earlier studies that CeF_3 responds non-proportionally to gamma rays up to 5.1 MeV [48,49]. Nonetheless, the analysis of CeF_3 monocrystals demonstrates that they are appropriate for high-rate calorimetry. Tests utilizing CeF_3-based prototype calorimeters (such as the high-luminosity Large Hadron Collider, HL-LHC) demonstrated encouraging results in terms of energy resolution [36–38].

According to recent studies, a CeF_3 crystal is an excellent Faraday rotator for broadband high-precision spectroscopy, particularly suitable for high-power laser applications [40,50–52]. This material appears with better characteristics than the commercial TGG crystal in terms of transparency in the UV-NIR region [46]. Additionally, a CeF_3 mono-crystal as an optical isolator is an advantageous alternative for protecting laser devices from back reflection, particularly in the UV-NIR wavelength ranges [40,46,50].

An essential disadvantage of a CeF_3 inorganic scintillator is that it tends strongly to overlap the luminescence band with the absorption cutoff, which is due to the fact that the Stokes shift is small and the material is a self-activated scintillator [39–41,43,44,46–49,53,54].

The aim of this work was to experimentally assess the general performance (emission efficiency and spectral compatibility with optical sensors) of a CeF_3 crystal under conditions found in medical laboratories as well as in various other applications such as industrial, geological, archeological, in security, etc. Most of these applications use mainly continuous spectrum X-rays produced by suitable X-ray tubes.

The findings of this work were compared with a $CeBr_3$ crystal that was recently examined by our group as well as to a crystal that has been incorporated in commercially available nuclear medicine scanners, i.e., bismuth germanate ($Bi_4Ge_3O_{12}$-BGO) [1,55]. The properties of the three materials are shown in Table 1.

Table 1. Properties of CeF_3, $CeBr_3$ and BGO single crystals [1,18,19,26,39,40,56–75].

	Units	CeF_3	$CeBr_3$	BGO
Wavelength of max emission	Nm	340 (slow), 300–310 (fast) [40,68]	380 [1,18]	480 [19,74]
Emission wavelength range	Nm	250–425 [68]	325–475 [1]	375–650 [1]
Decay times	Ns	30 (slow), 8 (fast) [40]	19 [1,18]	300 [19,56]
Light yield	photons/MeV	4.4×10^3 [40]	6×10^4 [1,18,26]	8.9×10^3 [19]
Photoelectron yield	% of NaI:Tl	8 [68]	122 [1]	15–20 [74]
Radiation length	Cm	1.654 [68]	1.96 [1]	1.12 [76]
Refractive index @ max nm		1.62 @ 440 nm [40]	2.09 @ 340 nm [1]	2.15 @ 480 nm [77]
Density	g/cm³	6.16 [40]	5.1 [1]	7.13 [19]

Table 1. *Cont.*

	Units	CeF_3	$CeBr_3$	BGO
Melting point	°C	1443–1450 [39,40,71]	722 [1]	1050 [74]
Mechanical hardness	Mohs	4.5–5 [39]	5–6 [1]	5 [78]
Radiation hardness	Rad	$>10^6$ [73]	2×10^3 [1]	10^7 [79]
Hygroscopic		No [40]	Yes [1,18]	No [19]

2. Results

Figure 1 shows the signal reading produced by the CeF_3 crystal, after X-ray irradiation, compared to the X-ray exposure rate. In the same Figure can be seen the output signal of the $CeBr_3$ and BGO crystals, under similar irradiation conditions. All the crystal samples had a purity of >99.99% (personal communication with Advatech (London, UK). From Figure 1, it can be depicted that the output signal and the exposure rate of the medical X-ray tube can be considered linear in the examined energy range (0 to 372 mR/s), except for $CeBr_3$ where linearity is lost for less than 50 mR/s. However, the replacement of bromine with fluorine in $CeBr_3$ results in a significant reduction in the signal output curve (from 29.54 in $CeBr_3$ to 0.834 in CeF_3). The output signal of BGO, which is a commercially available crystal in medical imaging applications, is also greater than that of CeF_3, denoting that CeF_3 has a low light yield for medical applications in the energy range 50–140 kVp.

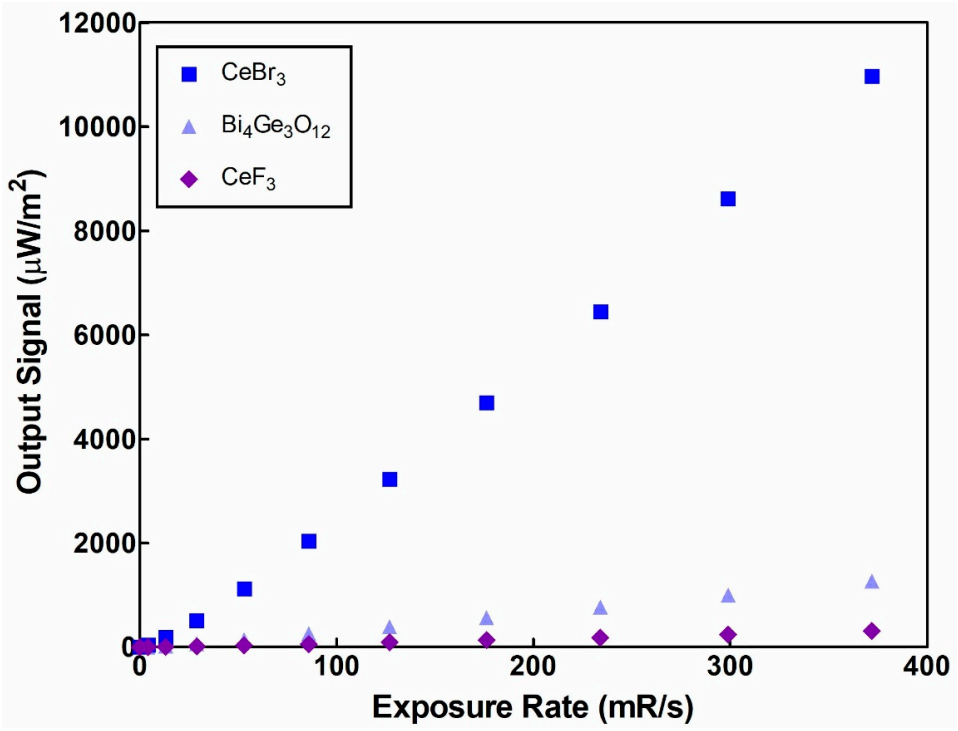


Figure 1. CeF_3's output signal compared to $CeBr_3$ and BGO.

Figure 2 shows the experimental results regarding the absolute luminescence efficiency of CeF_3 compared to the $CeBr_3$ and $Bi_4Ge_3O_{12}$ crystals. The results are shown for the available kVp of the X-ray tube, with steps of 10 kVp. A common finding, for the three examined crystals, is that in the examined X-ray range, the luminescence efficiency increases when the tube voltage increases. The increase in the luminescence efficiency is more evident in the range 50–80 kVp, due to the fact that the K-edges of all three materials are in this energy range. CeF_3 reaches a maximum value of only 0.8334 EU (EU is the S.I. equivalent $\mu Wm^{-2}/(mGy/s)$ at 140 kVp), whereas the corresponding values for $CeBr_3$ and BGO are

29.49 and 3.41, respectively, despite the higher density (6.16 compared to 5.1 g/cm^3) of CeF_3 compared with $CeBr_3$ (Table 1) [1]. Luminescence efficiency measurements in higher available X-ray energies could reveal a more efficient performance that possibly fulfils the requirements for nuclear medicine applications.

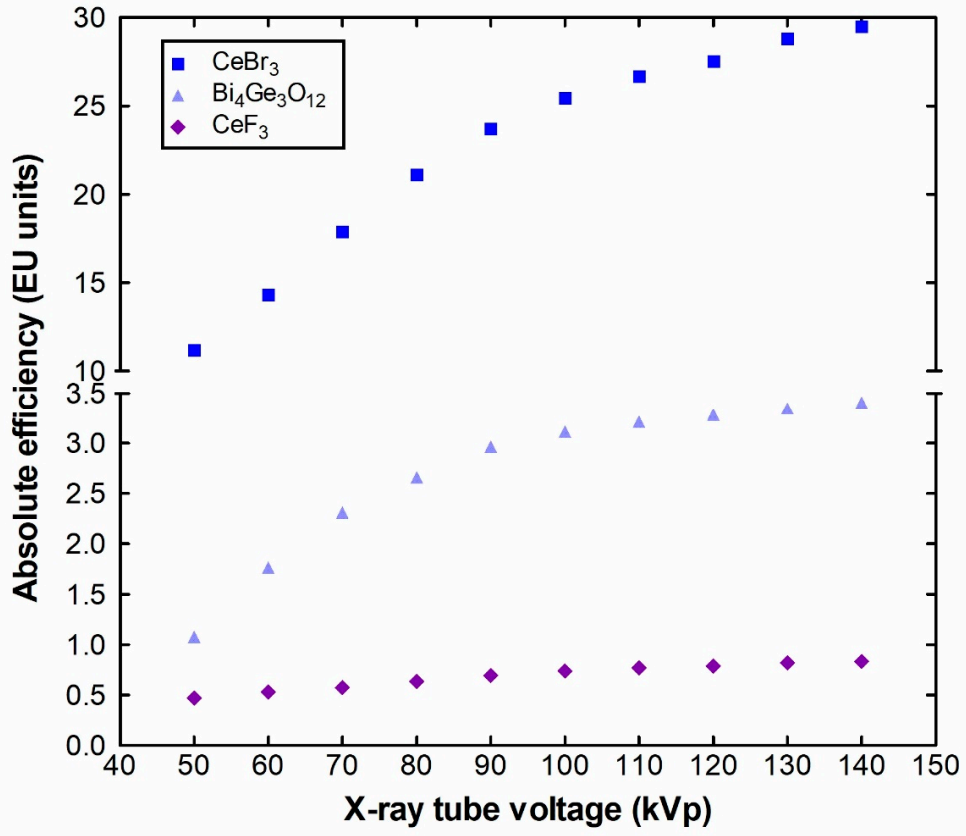


Figure 2. CeF_3's absolute luminescence efficiency compared to $CeBr_3$ and BGO.

Figure 3 shows the spectral matching values of CeF_3 with a broad variety of optical sensors. The emission spectrum of CeF_3 in the range of 260–400 nm and with an emission maximum at around 313 nm, which shifted to the shortwave region by 67 nm compared to $CeBr_3$, limits the available sensors commonly used in medical imaging applications that could be coupled with, such as charge coupled devices (CCDs) or complementary metal oxide semiconductors (CMOS) [80].

The main luminescence mechanism, observed in the CeF_3 crystal, is mainly due to 5d-4f transitions of the cerium (Ce^{3+}) ions [25]. Electron transitions from the 4f to the 5d energy level occur when these ions (CeF_3) are excited. The return of electrons to the 4f state produces photons. Due to this mechanism, the two primary luminescence bands of the crystal are created. These bands are located at around 290 nm and 340 nm, respectively [25,81,82]. Previous studies have demonstrated an association between the emission at 290 nm and the 5d-4f transitions in cerium (Ce^{3+}) ions. This band is produced by the electrons that radiatively decay from the excited 5d ground state to the 4f ground state [25,81,82]. Frenkel self-trapped excitons are produced as a result of the presence of sub bands in the conduction band, which are obtained from the 5d states of the ions and provide the procedure of the luminescence [25,43–45]. The electronic structure and the luminescence mechanism of CeF_3 crystal are valuable in evolving scintillators for radiological applications and for other applications in high-energy physics [40,46,47,50–52].

As can be depicted from Figure 3, the spectral matching factors between CeF_3 and most of the CCDs and CMOS are close to zero. However, CeF_3 can be matched with a variety of optical sensors, such as silicon (SiPMs), position-sensitive photomultipliers,

etc., which are used in nuclear medicine applications [83,84]. For example, the emission spectrum of CeF_3 has a 97% match with the spectral sensitivity of multialkali photocathodes and flat-panel position-sensitive (PS) photomultipliers (H8500D-03) (for both, the spectral matching factor is 0.97). Lower compatibility values can be found with gallium arsenide (GaAs) photocathodes (α_s = 0.8) and the extended (E-S20) photocathode used to measure the luminescence efficiency signal in this work (α_s = 0.76). This value is also used for the calculation of the AE.

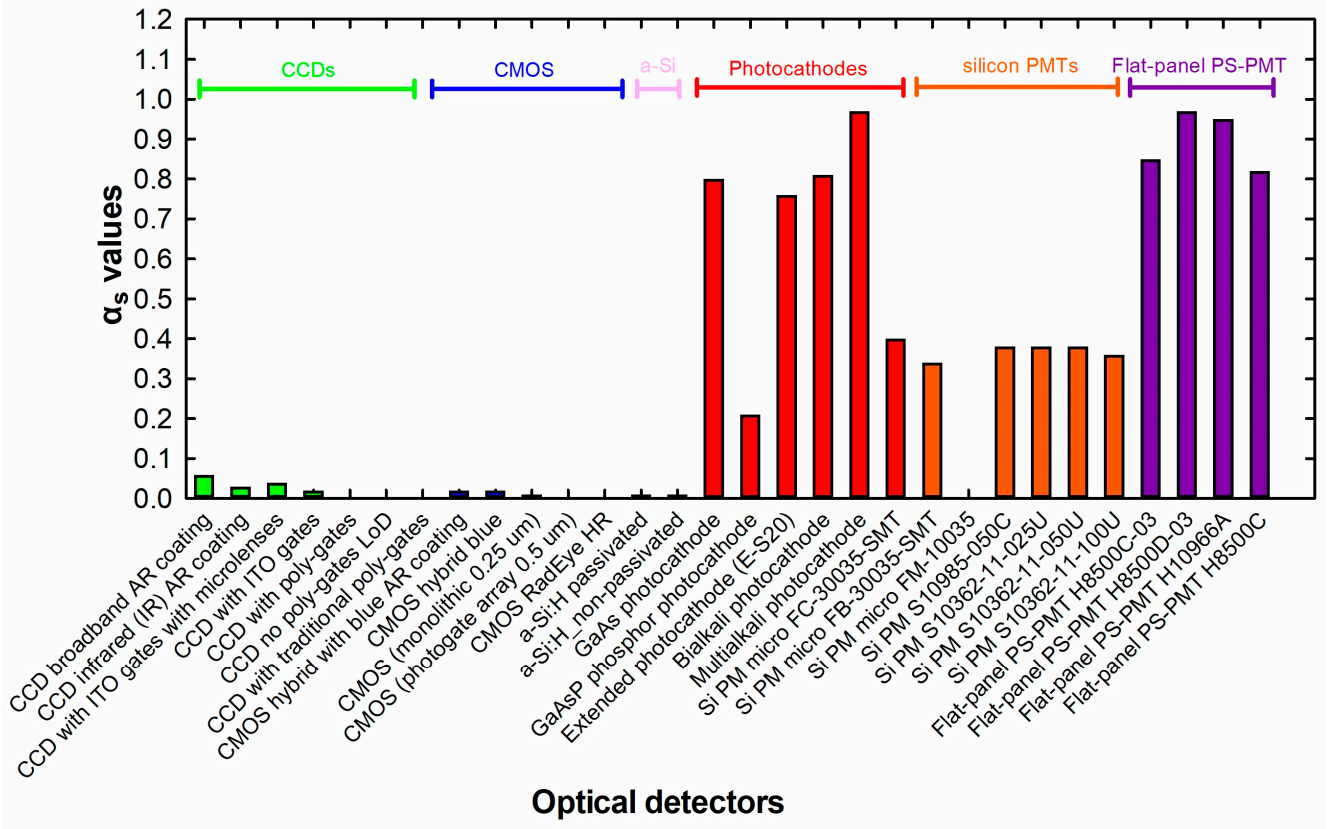


Figure 3. CeF_3 inorganic crystal's spectral matching factors with a series of digital optical detectors available for medical imaging applications.

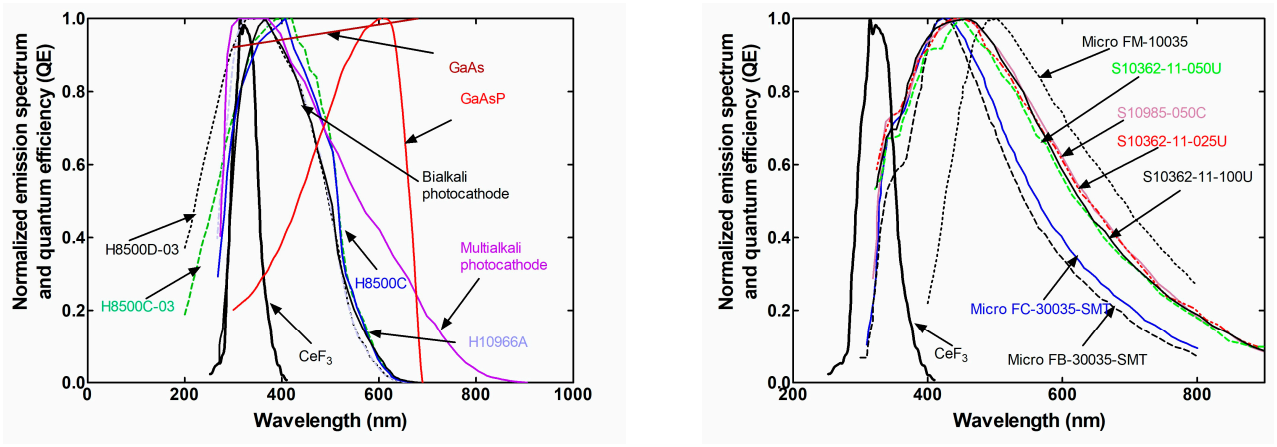
The spectral responses that were used for the calculation of the α_s between CeF_3 with a series of light sensors are shown in Figures 4 and 5, along with the emitted spectrum of CeF_3 [68]. Figure 4 shows the grouped spectral responses of the photocathodes (Figure 4a) and silicon photomultipliers (Figure 4b), whereas Figure 5 shows the grouped spectral responses of the CCDs (Figure 5a) and CMOS (Figure 5b).

The CeF_3 spectral matching results, presented in the spectral matching factors data of Figure 3, were used to calculate the EE that could be produced upon coupling the specific crystal with the examined optical sensors. Figures 6 and 7 show the calculated effective luminescence efficiency values with the X-ray tube voltage for the above-mentioned optical sensors. Figure 6 shows the grouped spectral responses of the photocathodes (Figure 6a) and silicon photomultipliers (Figure 6b), whereas Figure 7 shows the grouped spectral responses of the CCDs (Figure 7a) and CMOS (Figure 7b).

Following the spectral matching factor results, the effective efficiency is maximized for multialkali photocathodes and flat-panel position-sensitive photomultipliers, since in these cases, most of the emitted light from the CeF_3 scintillator can be adequately collected by the detectors.

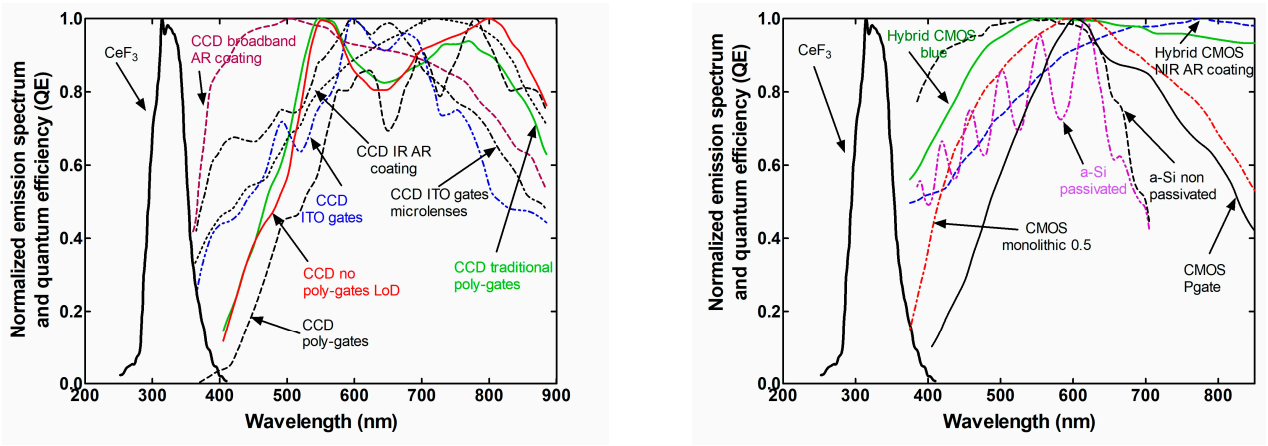
The combination of the multialkali photocathode with CeF_3 results in the effective efficiency values being reduced by 2.58% compared to the absolute efficiency values at

140 kVp. In the case of the combination of CeF_3 with the gallium arsenide photocathode, the corresponding absolute efficiency reduction is 24.26% at 140 kVp.



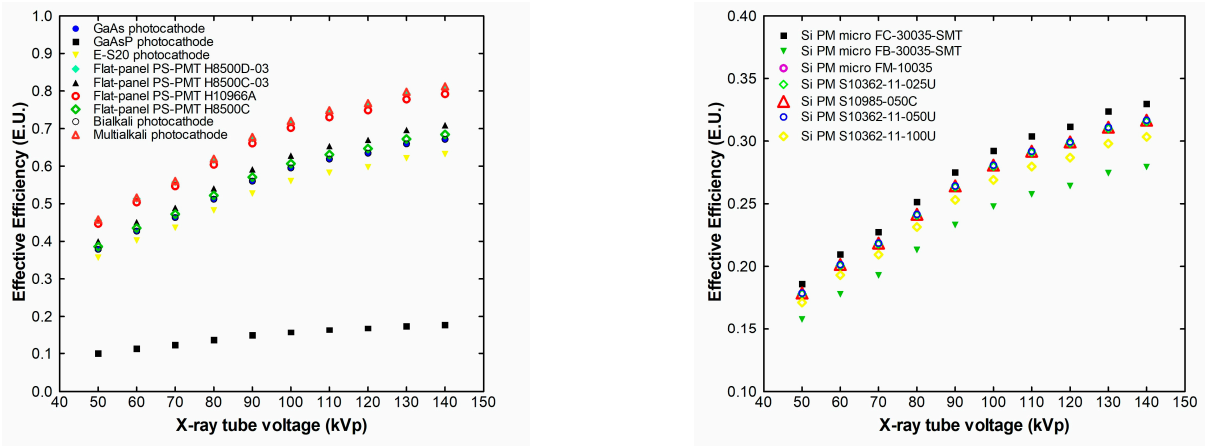
(**a**) (**b**)

Figure 4. Spectral responses of (**a**) photocathodes and (**b**) silicon PMs, along with the emission spectrum of CeF_3.



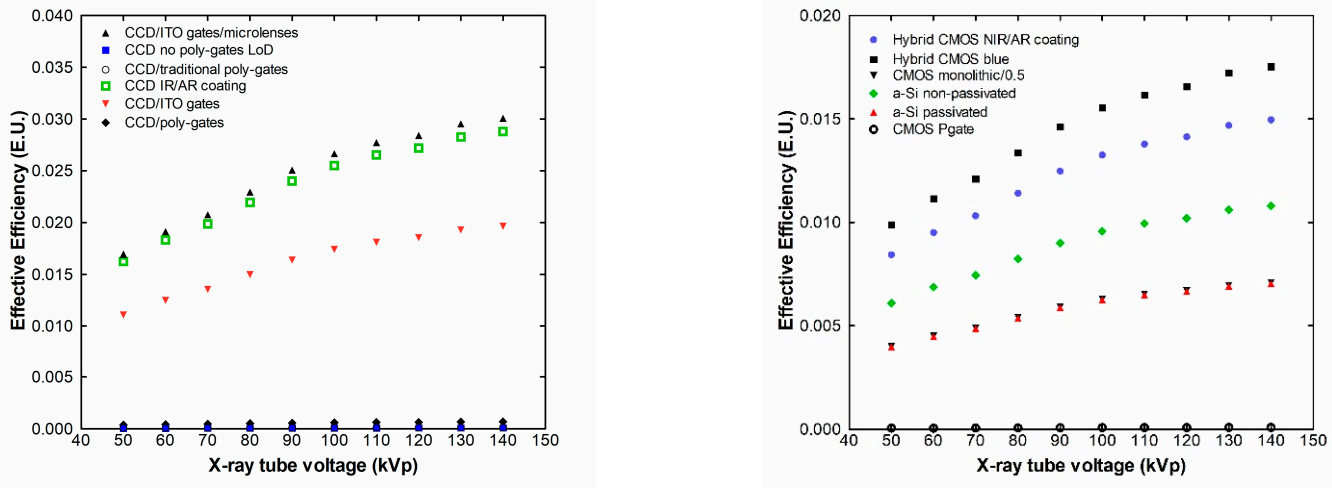
(**a**) (**b**)

Figure 5. Spectral responses of (**a**) CCDs and (**b**) CMOS, along with the emission spectrum of CeF_3.



(**a**) (**b**)

Figure 6. Effective luminescence efficiency of CeF_3 with photocathodes (**a**) and silicon PMTs (**b**).



(**a**) (**b**)

Figure 7. Effective luminescence efficiency of CeF_3 with CCDs (**a**) and CMOS (**b**).

Typical EE values for single-crystal scintillators, already integrated in medical imaging systems, range from 3 EE for BGO (used, for example, in the GE Discovery IQ scanner, GE Healthcare, Milwaukee, WI, USA) [85], 5 EE for GSO:Ce (Philips Gemini GXL PET/CT, Philips Medical Systems, Eindhoven, The Netherlands) [86], 8 for LYSO:Ce (Philips Gemini TF PET/CT, Philips Medical Systems, Eindhoven, The Netherlands) [87] to 12 for LSO:Ce (Siemens Biograph TruePoint PET/CT, Siemens Healthineers, Forchheim, Germany) [88,89].

Figure 8 shows the X-ray luminescence efficiency of the CeF_3 crystal compared to the data for $CeBr_3$ and BGO, in the examined X-ray tube voltage range. The XLE is an important parameter for detectors that are operated as energy integrators. This type of sensor is used in medical imaging systems, in which the signal output is related to the amount of energy that is captured by the crystal. The CeF_3 XLE values are below the corresponding ones for $CeBr_3$ and BGO as was expected from the previous findings (Figures 1 and 2). They start from 3.2×10^{-4} at 50 kVp and drop down to 2.3×10^{-4} at 140 kVp. The corresponding values for $CeBr_3$ and BGO were 7.6×10^{-3} and 7.3×10^{-4} at 50 kVp, reaching a maximum of 8.9×10^{-3} ($CeBr_3$ at 90 kVp) and 1.1×10^{-3} (BGO at 80 kVp) and afterwards, both drop down to 8.2×10^{-3} and 9.4×10^{-4} at 140 kVp, respectively. In the case of CeF_3, even the characteristic K-edge (at ~40 keV as shown in Figure 9) does not contribute to an XLE increase, like in the case of $CeBr_3$, with a K-edge at almost the same energy with CeF_3 (~40 keV) or BGO (~90.5 keV).

Figure 9 shows the calculated attenuation coefficients (μ_{att}) and the energy absorption (μ_{en}) coefficients of CeF_3, $CeBr_3$ and BGO, in the energy range 8 to 150 keV. The elemental coefficients (cerium, fluorine, bromine, bismuth (Bi), germanium (Ge) and oxygen (O)) that were used to calculate the CeF_3, $CeBr_3$ and BGO mixtures were obtained from the NIST XmuDat database [90,91]. The decrease in the coefficients, except from the sudden increase due to the characteristic K-absorption, for every mixture point, where the probability of photoelectric interaction maximizes, can also be seen in Figure 9.

Figure 10 shows the EAE values of CeF_3 compared to $CeBr_3$ and BGO. The energy absorption efficiency strongly depends on the μ_{en} and μ_{att} coefficients, shown in Figure 9, as well as on their ratio (μ_{en}/μ_{att}, Equation (4)), shown as an inset in Figure 10. Initially, for energies up to 39 keV, CeF_3 maintained a higher attenuation coefficient ratio than both $CeBr_3$ and BGO, leading to a higher energy absorption efficiency value at 40 kVp. However, when the energy increases, the energy absorption of BGO showed superior energy absorption efficiency values across the examined energy range, due to the combined effects of the density, higher μ_{en}/μ_{att} ratio (from 39 to 90 keV) and the increase in absorption due to the K-edge. Both $CeBr_3$ and CeF_3 have close attenuation coefficient values due to the presence of cerium (gram atomic mass = 140.116 g/mol) in both crystals; however, the

influence of the three atoms of bromine (gram atomic mass = 79.904 g/mol) is stronger than the corresponding three atoms of fluorine (gram atomic mass = 18.998 g/mol), leading to a gram molecular mass for CeF_3 equal to 197.111 g/mol compared to 172.549 g/mol for $CeBr_3$. After the K-edge absorption, CeF_3 exhibits a lower μ_{en}/μ_{att} ratio and consequently lower EAE values up to 129 keV across the examined energy range.

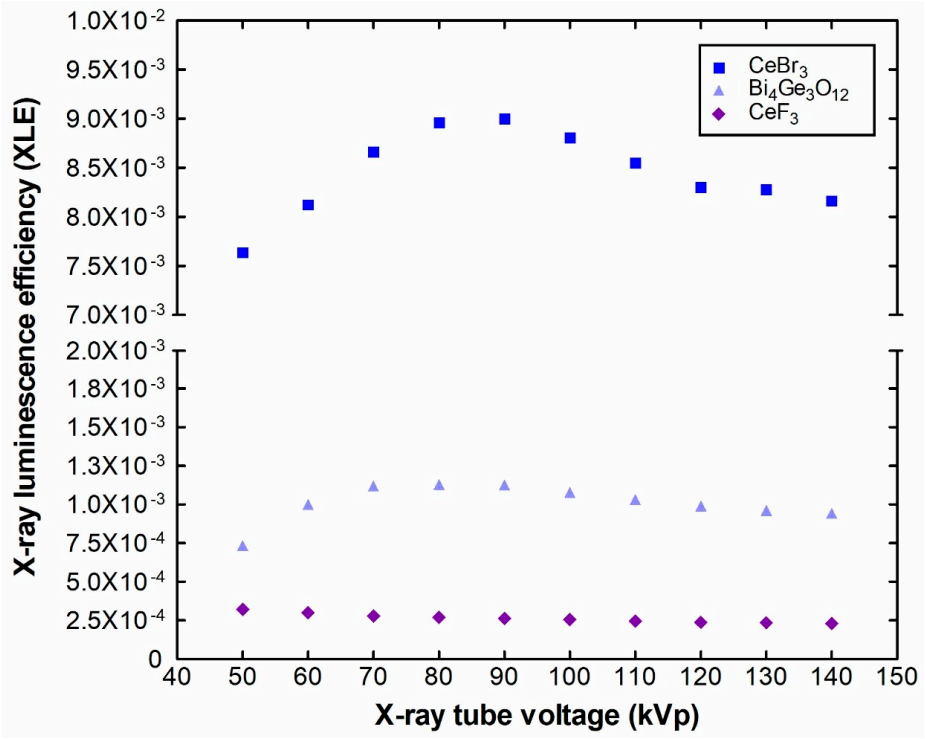


Figure 8. XLE of CeF_3 compared to $CeBr_3$ and BGO.

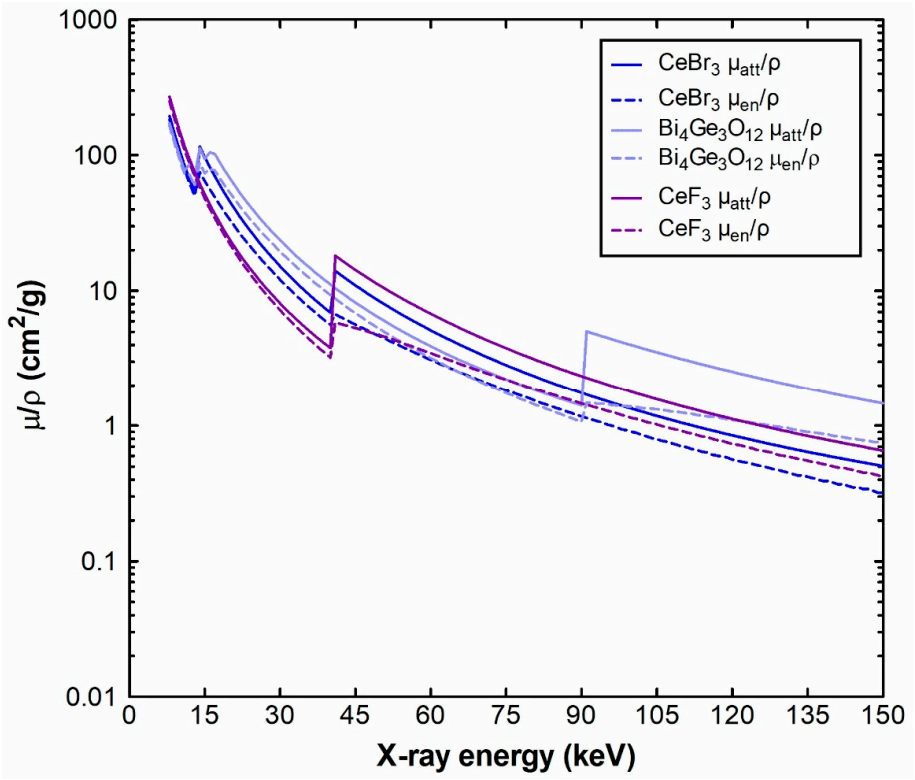


Figure 9. Mass attenuation coefficients of CeF_3 compared to $CeBr_3$ and BGO.

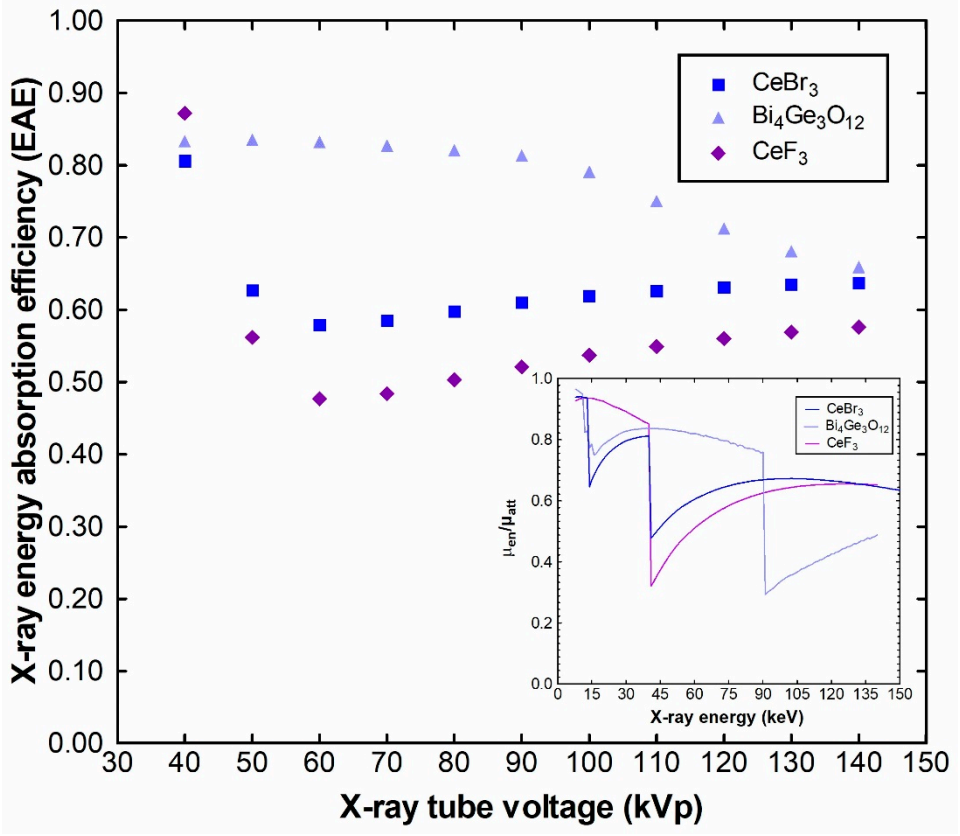


Figure 10. Energy absorption efficiency and μ_{en}/μ_{att} ratios of CeF_3 compared to $CeBr_3$ and BGO.

3. Materials and Methods

The cubic-shaped (edge of 10 mm) and polished CeF_3 crystal was obtained from Advatech (London, UK) [68]. For the irradiation of the sample, a typical radiological X-ray tube (CPI Inc., Georgetown, ON, Canada, model CMP 200 DR high-frequency X-ray generator and an X-ray tube (IAE SpA, Milano, Italy, model SpA-RTM90HS) was used, with voltage settings of 50–140 kVp, tube current fixed at 63 mAs, large focus (1.2 mm), a source to detector distance of 72.5 cm and an additional aluminum (Al) filter with a thickness of 20 mm.

The emitted light energy produced by the crystals per unit area (Ψ_Λ) was determined as the output signal in the energy range that diagnostic medical X-ray tubes allow (50–140 kVp). The methodology is described in detail in [1].

The CeF_3 sample was wrapped with Teflon tape (only one face was free) and inserted in the input port of an integrating sphere ((Newport Corp., Irvine, CA, USA, Oriel model 70451). The light that was produced by the sample, after X-ray excitation, was collected by a photomultiplier tube (PMT, (EMI, London, UK, EMI model 9798). The PMT's photocathode was the extended sensitivity (S20) type. The dose was monitored using an RTI Piranha P100B dosimeter (Mölndal, Sweden). In our experiments, the PMT works with a 22 volts difference between the initial dynode (all dynodes shorted) and the photocathode. The produced current is recorded by a sub-femtoamp remote source meter (Keithley, Cleveland, OH, USA, model 6430).

The ratio of the light energy flux emitted by the examined sample, normalized by the X-ray exposure rate, can be expressed as the absolute luminescence efficiency:

$$AE = \eta_A = \frac{\Psi_\Lambda}{X} = \left(\frac{i_{elec}}{S\eta_p\alpha_s c_g}\right)\dot{X}^{-1}, \quad (1)$$

In Equation (1), Ψ_Λ is the light energy flux (output signal) in units of $\mu W\ m^{-2}$. X is the exposure rate ($mR\ s^{-1}$). i_{elec} is the current produced by the electrometer in pA and S denotes

the surface of the crystal, excited by X-rays (mm^2). The peak sensitivity of the photocathode (η_p) is expressed in units of pA/W. α_s is the spectral matching between the light source (in this case, crystal) to the spectral response of the optical sensor (in this case, the photocathode). Finally, the percentage of the sample's emitted light escaping the integrating sphere and reacting with the PMT is the geometric light collection efficiency (c_g) with a measured value of 15.6. The units of the luminescence efficiency are EU = ($\mu W\ m^{-2}$)/($mR\ s^{-1}$). The experimental error is within $\pm 3.4\%$ due to the combined effects of the reproducibility of the X-ray tube output and optical measurement setups.

If the AE is reduced by the spectral matching factor (α_s) (denoting the percent of the light produced by the scintillator, which is within the same wavelength range as the optical response of a light sensor), then the effective efficiency is derived [1]:

$$EE = \eta_{eff} = \eta_A \alpha_s \tag{2}$$

The effective efficiency was calculated for various optical detectors, often used in medical applications, while the spectrum of CeF_3 was obtained from manufacturer data [68].

The X-ray luminescence efficiency (XLE) is the ratio of the crystal's emitted light energy flux over the X-ray energy flux ($\eta_\Psi = \Psi_\Lambda / \Psi_0$) [1].

Calculation of the XLE can be performed by the conversion of the X-ray exposure (in Equation (1)) to the X-ray energy flux (Ψ_o), using $\Psi_o = X\hat{\Psi}$ where $\hat{\Psi}$ is the X-ray energy flux per exposure rate:

$$\hat{\Psi} = \frac{\int \Psi_0(E)dE}{\int \Psi_0(E)\left[\frac{X}{\Psi_0(E)}\right]dE} = \frac{\int \Psi_0(E)dE}{\int \Psi_0(E)\left[\left(\frac{\mu_{en}(E)}{\rho}\right)_{air} \cdot \left(\frac{W_A}{e}\right)^{-1}\right]dE} \tag{3}$$

$(\mu_{en}(E)/\rho)_{air}$ is the X-ray mass energy absorption coefficient of the air and W_A/e is the average energy/unit of charge, for the production of an electron/ion pair in the air.

The energy absorption efficiency is used to account for the energy locally absorbed at the points of X-ray interaction, within the crystal [1]:

$$EAE(E) = \frac{\int_0^{E_0} \Phi_0(E) E \left(\frac{\mu_{en}(E)/\rho}{\mu_{att}(E)/\rho}\right)\left(1 - e^{-(\mu_{att}(E)/\rho)\rho W}\right)dE}{\int_0^{E_0} \Phi_0(E) E dE} \tag{4}$$

In Equation (4), the X-ray photon fluence is depicted by $\Phi_0(E)$ in units of photons/unit of area and is multiplied by the energy of the photons (E), in order to reproduce the X-ray energy fluence. The X-ray mass attenuation ($\mu_{att}(E)/\rho$) and the energy absorption coefficients ($\mu_{en}(E)/\rho$) were calculated from the NIST XmuDat database [90,91]. The crystal thickness is denoted by W and the density by ρ, in units of g/cm^3 [92].

4. Conclusions

This study aimed to investigate the luminescence properties of a CeF_3 single-crystal inorganic scintillator as a possible alternative to high-luminous but hygroscopic $CeBr_3$. The experiments were performed under the exposure of a typical X-ray unit, with X-rays spanning from 50 to 140 kVp. The fluorine in CeF_3 appeared to drastically reduce the luminescence efficiency, compared to the $CeBr_3$ crystal and other commercially used crystals in medical applications such as BGO. Furthermore, the emission maximum moved even lower than $CeBr_3$, towards the lower part of the visible spectrum and beyond, making CeF_3 suitable for spectral coupling with some multialkali photocathodes and flat-panel position-sensitive photomultipliers applied in nuclear medicine detectors, but completely unsuitable for spectral matching with CCDs and CMOS, used in a variety of medical imaging sensors. The obtained luminescence efficiency results denote that CeF_3 cannot be applied in medical imaging applications, covering the range 50–140 kVp; however, examination of its luminescence efficiency at higher energies could reveal a possible applicability for nuclear medicine detectors.

Author Contributions: Conceptualization, C.M. and V.N.; methodology, C.M., V.N., I.V., N.K., G.F. and I.K.; software, V.N.; validation, N.K. and I.K.; formal analysis, C.M., N.K. and V.N.; investigation, C.M., N.K., G.F., V.N., A.B. and I.V.; resources, A.B.; data curation, C.M., N.K., V.N., G.F. and I.K.; writing—original draft preparation, V.N. and C.M.; writing—review and editing, C.M., I.K., N.K., A.B. and I.V.; visualization, I.V.; supervision, C.M.; project administration, C.M. and I.V. All authors have read and agreed to the published version of the manuscript.

Funding: This research received no external funding.

Data Availability Statement: Data are contained within the article.

Conflicts of Interest: The authors declare no conflicts of interest.

References

1. Linardatos, D.; Michail, C.; Kalyvas, N.; Ninos, K.; Bakas, A.; Valais, I.; Fountos, G.; Kandarakis, I. Luminescence Efficiency of Cerium Bromide Single Crystal under X-ray Radiation. *Crystals* **2022**, *12*, 909. [CrossRef]
2. Zou, Z.; Weng, J.; Liu, C.; Lin, Y.; Zhu, J.; Sun, Y.; Huang, J.; Gong, G.; Wen, H. Crystal Growth, Photoluminescence and Radioluminescence Properties of Ce^{3+}-Doped $Ba_3Y(PO_4)_3$ Crystal. *Crystals* **2024**, *14*, 431. [CrossRef]
3. Ciomaga Hatnean, V.C.; Pui, A.; Simonov, A.; Ciomaga Hatnean, M. Crystal Growth of the R_2SiO_5 Compounds (R = Dy, Ho, and Er) by the Floating Zone Method Using a Laser-Diode-Heated Furnace. *Crystals* **2023**, *13*, 1687. [CrossRef]
4. Sahani, R.M.; Pandya, A. Novel Epoxy-bPBD-BisMSB Composite Plastic Scintillator for Alpha, Beta and Gamma Radiation Detection. *Sci. Rep.* **2024**, *14*, 6531. [CrossRef] [PubMed]
5. Pagano, F.; Král, J.; Děcká, K.; Pizzichemi, M.; Mihóková, E.; Čuba, V.; Auffray, E. Nanocrystalline Lead Halide Perovskites to Boost Time-of-Flight Performance of Medical Imaging Detectors. *Adv. Mater. Interfaces* **2024**, *11*, 2300659. [CrossRef]
6. Lai, Z.; Wang, W.; Liu, F.; Liu, Z.; Wang, S.; Lai, J.; Chen, J.; Zhang, H.; Xu, R.; Wang, L. High-Quality CsI(Tl) Single-Crystal Flake Scintillators Grown by the Space-Confined Solution Method. *Opt. Mater.* **2024**, *151*, 115333. [CrossRef]
7. Mahato, S.; Makowski, M.; Bose, S.; Kowal, D.; Kuddus Sheikh, M.A.; Braueninger-Wemer, P.; Witkowski, M.E.; Ray, S.K.; Drozdowski, W.; Birowosuto, M.D. Improvement of Light Output of $MAPbBr_3$ Single Crystal for Ultrafast and Bright Cryogenic Scintillator. *J. Phys. Chem. Lett.* **2024**, *15*, 3713–3720. [CrossRef]
8. Glodo, J.; van Loef, E.; Wang, Y.; Bhattacharya, P.; Pandian, L.S.; Shirwadkar, U.; Hubble, I.; Schott, J.; Muller, M. Novel High-Stopping Power Scintillators for Medical Applications. In Proceedings of the Medical Imaging 2024: Physics of Medical Imaging, SPIE, San Diego, CA, USA, 1 April 2024; Volume 12925, pp. 585–595.
9. Nazarov, M.; Tsukerblat, B. Optical Lines in Europium and Terbium-Activated Yttrium Tantalate Phosphor: Combined Experimental and Group-Theoretical Analysis. *Optics* **2023**, *4*, 510–524. [CrossRef]
10. Komendo, I.; Mechinsky, V.; Fedorov, A.; Dosovitskiy, G.; Schukin, V.; Kuznetsova, D.; Zykova, M.; Velikodny, Y.; Korjik, M. Effect of the Synthesis Conditions on the Morphology, Luminescence and Scintillation Properties of a New Light Scintillation Material Li_2CaSiO_4:Eu^{2+} for Neutron and Charged Particle Detection. *Inorganics* **2022**, *10*, 127. [CrossRef]
11. Cheng, Y.; Huang, Y.; Yu, G. N-S-Co-Doped Carbon Dot Blue Fluorescence Preparation and Baicalein Detection. *Inorganics* **2024**, *12*, 154. [CrossRef]
12. Higgins, W.M.; Churilov, A.; van Loef, E.; Glodo, J.; Squillante, M.; Shah, K. Crystal Growth of Large Diameter $LaBr_3$:Ce and $CeBr_3$. *J. Cryst. Growth* **2008**, *310*, 2085–2089. [CrossRef]
13. Wei, H.; Martin, V.; Lindsey, A.; Zhuravleva, M.; Melcher, C.L. The Scintillation Properties of $CeBr_{3-x}Cl_x$ Single Crystals. *J. Lumin.* **2014**, *156*, 175–179. [CrossRef]
14. Loyd, M.; Stand, L.; Rutstrom, D.; Wu, Y.; Glodo, J.; Shah, K.; Koschan, M.; Melcher, C.L.; Zhuravleva, M. Investigation of $CeBr_{3-x}I_x$ Scintillators. *J. Cryst. Growth* **2020**, *531*, 125365. [CrossRef]
15. Kandarakis, I. Luminescence in Medical Image Science. *J. Lumin.* **2016**, *169*, 553–558. [CrossRef]
16. Madej, A.; Witkowski, M.E.; Wojtowicz, A.J.; Zych, E. Photo- and Radioluminescent Properties of Undoped and Bi-Doped Lu_2WO_6 Powders at 10–300K. *J. Lumin.* **2015**, *160*, 50–56. [CrossRef]
17. Xie, S.; Zhang, X.; Zhang, Y.; Ying, G.; Huang, Q.; Xu, J.; Peng, Q. Evaluation of Various Scintillator Materials in Radiation Detector Design for Positron Emission Tomography (PET). *Crystals* **2020**, *10*, 869. [CrossRef]
18. Koppert, W.J.C.; Dietze, M.M.A.; Velden, S.; Steenbergen, J.H.L.; Jong, H.W.A.M. A Comparative Study of NaI(Tl), $CeBr_3$ and CZT for Use in a Real-Time Simultaneous Nuclear and Fluoroscopic Dual-Layer Detector. *Phys. Med. Biol.* **2019**, *64*, 135012. [CrossRef] [PubMed]
19. Lecoq, P. Development of New Scintillators for Medical Applications. *Nucl. Instrum. Methods Phys. Res. Sect. Accel. Spectrom. Detect. Assoc. Equip.* **2016**, *809*, 130–139. [CrossRef]
20. Kim, K.J.; Furuya, Y.; Kamada, K.; Murakami, R.; Kochurikhin, V.V.; Yoshino, M.; Chiba, H.; Kurosawa, S.; Yamaji, A.; Shoji, Y.; et al. Growth and Scintillation Properties of Directionally Solidified Ce:$LaBr_3$/$AEBr_2$ (AE = Mg, Ca, Sr, Ba) Eutectic System. *Crystals* **2020**, *10*, 584. [CrossRef]

21. Carone, D.; Klepov, V.V.; Misture, S.T.; Schaeperkoetter, J.C.; Jacobsohn, L.G.; Aziziha, M.; Schorne-Pinto, J.; Thomson, S.A.J.; Hines, A.T.; Besmann, T.M.; et al. Luminescence and Scintillation in the Niobium Doped Oxyfluoride $Rb_4Ge_5O_9F_6$:Nb. *Inorganics* **2022**, *10*, 83. [CrossRef]
22. Linardatos, D.; Ntoupis, V.; Tseremoglou, S.; Valais, I.; Ninos, K.; Bakas, A.; Lavdas, E.; Kandarakis, I.; Kalyvas, N.; Fountos, G.; et al. Light Output Dependence of $CeBr_3$ Hygroscopic Scintillator upon Temperature. *Procedia Struct. Integr.* **2023**, *47*, 80–86. [CrossRef]
23. Li, P.; Gridin, S.; Ucer, K.B.; Williams, R.T.; Menge, P.R. Picosecond Absorption Spectroscopy of Self-Trapped Excitons and Ce Excited States in $CeBr_3$ and $La_{1-x}Ce_xBr_3$. *Phys. Rev. B* **2019**, *99*, 104301. [CrossRef]
24. Lecoq, P.; Gektin, A.; Korzhik, M. Scintillation and Inorganic Scintillators. In *Inorganic Scintillators for Detector Systems: Physical Principles and Crystal Engineering*; Lecoq, P., Gektin, A., Korzhik, M., Eds.; Springer International Publishing: Cham, Switzerland, 2017; pp. 1–41, ISBN 978-3-319-45522-8.
25. Kochan, O.; Chornodolskyy, Y.; Selech, J.; Karnaushenko, V.; Przystupa, K.; Kotlov, A.; Demkiv, T.; Vistovskyy, V.; Stryhanyuk, H.; Rodnyi, P.; et al. Energy Structure and Luminescence of CeF_3 Crystals. *Materials* **2021**, *14*, 4243. [CrossRef]
26. Przystupa, K.; Chornodolskyy, Y.M.; Selech, J.; Karnaushenko, V.O.; Demkiv, T.M.; Kochan, O.; Syrotyuk, S.V.; Voloshinovskii, A.S. The Influence of Halide Ion Substitution on Energy Structure and Luminescence Efficiency in $CeBr_2I$ and $CeBrI_2$ Crystals. *Materials* **2023**, *16*, 5085. [CrossRef]
27. Chornodolskyy, Y.M.; Karnaushenko, V.O.; Vistovskyy, V.V.; Syrotyuk, S.V.; Gektin, A.V.; Voloshinovskii, A.S. Energy Band Structure Peculiarities and Luminescent Parameters of CeX_3 (X = Cl, Br, I) Crystals. *J. Lumin.* **2021**, *237*, 118147. [CrossRef]
28. Russell-Webster, B.; Abboud, K.A.; Christou, G. Molecular Nanoparticles of Cerium Dioxide: Structure-Directing Effect of Halide Ions. *Chem. Commun.* **2020**, *56*, 5382–5385. [CrossRef]
29. Chipaux, R.; Faure, J.-L.; Rebourgeard, P.; Dauphin, G.; Safieh, J. Behaviour of CeF_3 Scintillator in an LHC-like Environment. *Nucl. Instrum. Methods Phys. Res. Sect. Accel. Spectrom. Detect. Assoc. Equip.* **1994**, *345*, 440–444. [CrossRef]
30. Schneegans, M.A. Cerium Fluoride Crystals for Calorimetry at LHC. *Nucl. Instrum. Methods Phys. Res. Sect. Accel. Spectrom. Detect. Assoc. Equip.* **1994**, *344*, 47–56. [CrossRef]
31. Ferrere, D.; Lebeau, M.; Schneegans, M.; Vivargent, M.; Lecoq, P. High Resolution Crystal Calorimetry at LHC. *Nucl. Instrum. Methods Phys. Res. Sect. Accel. Spectrom. Detect. Assoc. Equip.* **1992**, *315*, 332–336. [CrossRef]
32. Auffray, E.; Beckers, T.; Bourotte, J.; Chipaux, R.; Commichau, V.; Dafinei, I.; Depasse, P.; Djambazov, L.; Dydak, U.; El Mamouni, H.; et al. Performance of a Cerium Fluoride Crystal Matrix Measured in High-Energy Particle Beams. *Nucl. Instrum. Methods Phys. Res. Sect. Accel. Spectrom. Detect. Assoc. Equip.* **1996**, *378*, 171–178. [CrossRef]
33. Nikl, M.; Mares, J.A.; Dusek, M.; Lecoq, P.; Dafinei, I.; Auffray, E.; Pazzi, G.P.; Fabeni, P.; Jindra, J.; Skoda, Z. Decay Kinetics of Ce^{3+} Ions under Gamma and KrF Excimer Laser Excitation in CeF_3 Single Crystals. *J. Phys. Condens. Matter* **1995**, *7*, 6355. [CrossRef]
34. Auffray, E.; Beckers, T.; Chipaux, R.; Dafinei, I.; Depasse, P.; El Mamouni, H.; Faure, J.L.; Fay, J.; Hillemanns, H.; Ille, B.; et al. First Results on Large Cerium Fluoride Crystals in A Test Beam. *MRS Online Proc. Libr.* **1994**, *348*, 117–122. [CrossRef]
35. Pedrini, C.; Moine, B.; Bouttet, D.; Belsky, A.N.; Mikhailin, V.V.; Vasil'ev, A.N.; Zinin, E.I. Time-Resolved Luminescence of CeF_3 Crystals Excited by X-ray Synchrotron Radiation. *Chem. Phys. Lett.* **1993**, *206*, 470–474. [CrossRef]
36. Auffray, E.; Baccaro, S.; Beckers, T.; Benhammou, Y.; Belsky, A.N.; Borgia, B.; Boutet, D.; Chipaux, R.; Dafinei, I.; de Notaristefani, F.; et al. Extensive Studies on CeF_3 Crystals, a Good Candidate for Electromagnetic Calorimetry at Future Accelerators. *Nucl. Instrum. Methods Phys. Res. Sect. Accel. Spectrom. Detect. Assoc. Equip.* **1996**, *383*, 367–390. [CrossRef]
37. Inagaki, T.; Yoshimura, Y.; Kanda, Y.; Matsumoto, Y.; Minami, K. Development of CeF_3 Crystal for High-Energy Electromagnetic Calorimetry. *Nucl. Instrum. Methods Phys. Res. Sect. Accel. Spectrom. Detect. Assoc. Equip.* **2000**, *443*, 126–135. [CrossRef]
38. Bianchini, L.; Dissertori, G.; Donegà, M.; Lustermann, W.; Marini, A.; Micheli, F.; Nessi-Tedaldi, F.; Pandolfi, F.; Peruzzi, M.; Schonenberger, M.; et al. High-Energy Electron Test Results of a Calorimeter Prototype Based on CeF_3 for HL-LHC Applications. In Proceedings of the 2015 IEEE Nuclear Science Symposium and Medical Imaging Conference (NSS/MIC), San Diego, CA, USA, 31 October–7 November 2015; pp. 1–2.
39. Karimov, D.N.; Lisovenko, D.S.; Ivanova, A.G.; Grebenev, V.V.; Popov, P.A.; Sizova, N.L. Bridgman Growth and Physical Properties Anisotropy of CeF_3 Single Crystals. *Crystals* **2021**, *11*, 793. [CrossRef]
40. Víllora, E.G.; Yuan, D.; Shimamura, K. CeF_3 Single Crystals for UV-VIS-IR Optical Isolators. *Int. J. Appl. Ceram. Technol.* **2023**, *20*, 2047–2054. [CrossRef]
41. Yang, W.; Kong, X.; Fu, B.; Yang, Y.; Chen, R.; Zuo, C.; Liu, H.; Yu, Y.; Zeng, F.; Li, C. Optical Properties of CeF_3 Crystal at High Temperature or Pressure by First Principles and Its Application in Isolators. *Opt. Mater.* **2024**, *154*, 115758. [CrossRef]
42. Yuan, D.; Víllora, E.G.; Shimamura, K. Regular Hexagonal-Prism Microvoids in CeF_3 Single Crystals. *J. Cryst. Growth* **2021**, *558*, 126024. [CrossRef]
43. Chylii, M.; Loghina, L.; Kaderavkova, A.; Slang, S.; Rodriguez-Pereira, J.; Frumarova, B.; Vlcek, M. Morphology and Optical Properties of CeF_3 and CeF_3:Tb Nanocrystals: The Dominant Role of the Reaction Thermal Mode. *Mater. Chem. Phys.* **2021**, *260*, 124161. [CrossRef]
44. Zhu, L.; Li, Q.; Liu, X.; Li, J.; Zhang, Y.; Meng, J.; Cao, X. Morphological Control and Luminescent Properties of CeF_3 Nanocrystals. *J. Phys. Chem. C* **2007**, *111*, 5898–5903. [CrossRef]
45. Sizova, N.L.; Karimov, D.N.; Kosova, T.B.; Lisovenko, D.S. Mechanical Properties of CeF_3 Single Crystals. *Crystallogr. Rep.* **2019**, *64*, 942–946. [CrossRef]

46. Li, H.; Wang, J.; Chen, J.; Dai, Y.; Su, L.; Li, X.; Kalashnikova, A.M.; Wu, A. Bridgman Growth and Magneto-Optical Properties of CeF_3 Crystal as Faraday Rotator. *Opt. Mater.* **2020**, *100*, 109675. [CrossRef]
47. Kamenskikh, I.; Tishchenko, E.; Kirm, M.; Omelkov, S.; Belsky, A.; Vasil'ev, A. Decay Kinetics of CeF_3 under VUV and X-ray Synchrotron Radiation. *Symmetry* **2020**, *12*, 914. [CrossRef]
48. Klamra, W.; Sibczynski, P.; Moszynski, M.; Czarnacki, W.; Kozlov, V. Extensive Studies on Light Yield Non-Proportional Response of Undoped CeF_3 at Room and Liquid Nitrogen Temperatures. *J. Instrum.* **2013**, *8*, P06003. [CrossRef]
49. Thongpool, V.; Phunpueok, A.; Jaiyen, S.; Choosakul, N.; Aphairaj, D.; Thongchai, P.; Singhaseree, C. Preparation of CeF_3 Nanoparticles Loaded PPO/PVT Composites for Radiation Detection. *Dig. J. Nanomater. Biostructures* **2022**, *16*, 621–625. [CrossRef]
50. Lacy, J.H.; Patenotte, G.E.; Kinney, A.C.; Majumder, P.K. Broadband High-Precision Faraday Rotation Spectroscopy with Uniaxial Single Crystal CeF_3 Modulator. *Photonics* **2024**, *11*, 304. [CrossRef]
51. Starobor, A.; Mironov, E.; Palashov, O. High-Power Faraday Isolator on a Uniaxial CeF_3 Crystal. *Opt. Lett.* **2019**, *44*, 1297–1299. [CrossRef]
52. Vojna, D.; Slezák, O.; Yasuhara, R.; Furuse, H.; Lucianetti, A.; Mocek, T. Faraday Rotation of Dy_2O_3, CeF_3 and $Y_3Fe_5O_{12}$ at the Mid-Infrared Wavelengths. *Materials* **2020**, *13*, 5324. [CrossRef]
53. Lecoq, P. How High Energy Physics Is Driving the Development of New Scintillators. In Proceedings of the Fifth International Conference on Inorganic Scintillators and Their Applications, Moscow, Russia, 16–20 August 1999; CERN: Moscow, Russia, 1999.
54. Grynyov, B.; Ryzhikov, V.; Kim, J.K.; Jae, M. *Scintillator Crystals, Radiation Detectors & Instruments on Their Base*; V. Ryzhikov: Kharkiv, Ukraine, 2004; ISBN 966-02-3314-0.
55. Michail, C.; Liaparinos, P.; Kalyvas, N.; Kandarakis, I.; Fountos, G.; Valais, I. Phosphors and Scintillators in Biomedical Imaging. *Crystals* **2024**, *14*, 169. [CrossRef]
56. Valais, I.; Michail, C.; David, S.; Nomicos, C.D.; Panayiotakis, G.S.; Kandarakis, I. A Comparative Study of the Luminescence Properties of LYSO:Ce, LSO:Ce, GSO:Ce and BGO Single Crystal Scintillators for Use in Medical X-ray Imaging. *Phys. Med.* **2008**, *24*, 122–125. [CrossRef] [PubMed]
57. van Eijk, C.W.E. Inorganic Scintillators in Medical Imaging. *Phys. Med. Biol.* **2002**, *47*, R85–R106. [CrossRef]
58. Balcerzyk, M.; Moszynski, M.; Kapusta, M.; Wolski, D.; Pawelke, J.; Melcher, C.L. YSO, LSO, GSO and LGSO. A Study of Energy Resolution and Nonproportionality. *IEEE Trans. Nucl. Sci.* **2000**, *47*, 1319–1323. [CrossRef]
59. Kozma, P.; Kozma, P. Radiation Sensitivity of GSO and LSO Scintillation Detectors. *Nucl. Instrum. Methods Phys. Res. Sect. Accel. Spectrom. Detect. Assoc. Equip.* **2005**, *539*, 132–136. [CrossRef]
60. Holl, I.; Lorenz, E.; Mageras, G. A Measurement of the Light Yield of Common Inorganic Scintillators. *IEEE Trans. Nucl. Sci.* **1988**, *35*, 105–109. [CrossRef]
61. Passeri, A.; Formiconi, A.R. SPECT and Planar Imaging in Nuclear Medicine. In *Ionizing Radiation Detectors for Medical Imaging*; World Scientific: Singapore, 2004; pp. 235–285, ISBN 978-981-238-674-8.
62. Christian, J. Advances in CMOS SSPM Detectors. In *Biological and Medical Sensor Technologies*; Iniewski, K., Ed.; CRC Press: Boca Raton, FL, USA, 2017; p. 327, ISBN 978-1-138-07321-0.
63. Stolberg-Rohr, T.; Hawkins, G.J. Spectral Design of Temperature-Invariant Narrow Bandpass Filters for the Mid-Infrared. *Opt. Express* **2015**, *23*, 580. [CrossRef]
64. Rodnyj, P.A. Interaction of Ionizing Radiation with Scintillators. In *Physical Processes in Inorganic Scintillators*; The CRC Press Laser and Optical Science and Technology Series; CRC Press: Boca Raton, FL, USA, 1997; p. 17, ISBN 978-0-8493-3788-8.
65. Kawaguchi, N.; Kimura, H.; Nakauchi, D.; Kato, T.; Yanagida, T. Inorganic Fluoride Scintillators. In *Phosphors for Radiation Detectors*; John Wiley & Sons, Ltd.: Hoboken, NJ, USA, 2022; pp. 91–120, ISBN 978-1-119-58336-3.
66. van Loef, E.V.; Shah, K.S. Advances in Scintillators for Medical Imaging Applications. In Proceedings of the SPIE, San Diego, CA, USA, 12 September 2014; Barber, H.B., Furenlid, L.R., Roehrig, H.N., Eds.; p. 92140A.
67. Drozdowski, W.; Dorenbos, P.; Bos, A.J.J.; Owens, A.; Richaud, D. Gamma Radiation Hardness of Ø1″ × 1″ $LaBr_3$:Ce, $LaCl_3$:Ce, and $CeBr_3$ Scintillators. In Proceedings of the 2008 IEEE Nuclear Science Symposium Conference Record, Dresden, Germany, 19–25 October 2008; pp. 2856–2858.
68. CeF3—Cerium Fluoride Scintillator Crystal | Advatech UK. Available online: https://www.advatech-uk.co.uk/cef3.html (accessed on 2 May 2024).
69. CeBr3—Cerium Bromide Scintillator Crystal | Advatech UK. Available online: https://www.advatech-uk.co.uk/cebr3.html (accessed on 2 May 2024).
70. Shen, H.; Xu, J.Y.; Ping, W.J.; He, Q.B.; Zhang, Y.; Jin, M.; Jiang, G.J. Growth, Mechanical and Thermal Properties of $Bi_4Si_3O_{12}$ Single Crystals. *Chin. Phys. Lett.* **2012**, *29*, 076501. [CrossRef]
71. Cerium Fluoride Crystal CeF3 Scintillation Crystal–MSE Supplies LLC. Available online: https://www.msesupplies.com/products/cerium-fluoride-cef3-crystal?variant=40204171444282 (accessed on 7 June 2024).
72. Li, H.; Ge, W.; Li, J.; Dai, Y.; Chen, J.; Su, L.; Jin, Z.; Ma, G.; Li, X.; Wu, A. Temperature-Dependent Terahertz Dielectric Modulation of a High-Performance Magneto-Optic CeF_3 Crystal. *Phys. B Condens. Matter* **2020**, *599*, 412468. [CrossRef]
73. Kobayashi, M.; Ishii, M.; Krivandina, E.A.; Litvinov, M.M.; Peresypkin, A.I.; Prokoshkin, Y.D.; Rykalin, V.I.; Sobolev, B.P.; Takamatsu, K.; Vasil'chenko, V.G. Cerium Fluoride, a Highly Radiation-Resistive Scintillator. *Nucl. Instrum. Methods Phys. Res. Sect. Accel. Spectrom. Detect. Assoc. Equip.* **1991**, *302*, 443–446. [CrossRef]

74. Kozma, P.; Kozma, P. Radiation Resistivity of BGO Crystals Due to Low-Energy Gamma-Rays. *Nucl. Instrum. Methods Phys. Res. Sect. Accel. Spectrom. Detect. Assoc. Equip.* **2003**, *501*, 499–504. [CrossRef]
75. Snigireva, O.A.; Solomonov, V.I. Role of the Ce^{2+} Ions in Cerium Fluoride Luminescence. *Phys. Solid State* **2005**, *47*, 1443–1445. [CrossRef]
76. Yang, F.; Mao, R.; Zhang, L.; Zhu, R.-Y. A Study on Radiation Damage in BGO and PWO-II Crystals. *J. Phys. Conf. Ser.* **2012**, *404*, 012025. [CrossRef]
77. Sasano, M.; Nishioka, H.; Okuyama, S.; Nakazawa, K.; Makishima, K.; Yamada, S.; Yuasa, T.; Okumura, A.; Kataoka, J.; Fukazawa, Y.; et al. Geometry Dependence of the Light Collection Efficiency of BGO Crystal Scintillators Read out by Avalanche Photo Diodes. *Nucl. Instrum. Methods Phys. Res. Sect. Accel. Spectrom. Detect. Assoc. Equip.* **2013**, *715*, 105–111. [CrossRef]
78. Chaiphaksa, W.; Limkitjaroenporn, P.; Kim, H.J.; Kaewkhao, J. Moh's Hardness Scale and Micro Vicker's Hardness Study of Bgo and Lyso Inorganic Scintillators. *J. Phys. Conf. Ser.* **2018**, *970*, 012005. [CrossRef]
79. Kozma, P.; Bajgar, R.; Kozma, P. Radiation Resistivity of PbF_2 Crystals. *Nucl. Instrum. Methods Phys. Res. Sect. Accel. Spectrom. Detect. Assoc. Equip.* **2002**, *484*, 149–152. [CrossRef]
80. Magnan, P. Detection of Visible Photons in CCD and CMOS: A Comparative View. *Nucl. Instrum. Methods Phys. Res. Sect. Accel. Spectrom. Detect. Assoc. Equip.* **2003**, *504*, 199–212. [CrossRef]
81. Yang, Y.; Zhang, L.; Quan, C.; Li, S.; Zhang, S.; Zhang, Y.; Fang, Q.; He, M.; Xu, M.; Hang, Y. Growth, Thermal, and Polarized Spectroscopic Properties of Nd:CeF_3 Crystal for Dual-Wavelength Lasers. *J. Lumin.* **2020**, *227*, 117558. [CrossRef]
82. Shimamura, K.; Víllora, E.G.; Nakakita, S.; Nikl, M.; Ichinose, N. Growth and Scintillation Characteristics of CeF_3, PrF_3 and NdF_3 Single Crystals. *J. Cryst. Growth* **2004**, *264*, 208–215. [CrossRef]
83. Schaber, J.; Xiang, R.; Gaponik, N. Review of Photocathodes for Electron Beam Sources in Particle Accelerators. *J. Mater. Chem. C* **2023**, *11*, 3162–3179. [CrossRef]
84. MA, L.; Chen, L.; Huang, G.; Hu, J.; Han, X.; Hua, Z.; Huang, X.; Jin, M.; Jiang, X.; Jin, Z.; et al. The Time Resolution Improvement of Cherenkov-Radiator-Window Photomultiplier Tube. *J. Instrum.* **2023**, *18*, C12020. [CrossRef]
85. Ponti, E.D.; Crivellaro, C.; Morzenti, S.; Monaco, L.; Todde, S.; Landoni, C.; Elisei, F.; Musarra, M.; Guerra, L. Clinical Application of a High Sensitivity BGO PET/CT Scanner: Effects of Acquisition Protocols and Reconstruction Parameters on Lesions Quantification. *Curr. Radiopharm.* **2022**, *15*, 218–227. [CrossRef] [PubMed]
86. Sathiakumar, C.; Som, S.; Eberl, S.; Lin, P. NEMA NU 2-2001 Performance Testing of a Philips Gemini GXL PET/CT Scanner. *Australas. Phys. Eng. Sci. Med.* **2010**, *33*, 199–209. [CrossRef] [PubMed]
87. Surti, S.; Kuhn, A.; Werner, M.E.; Perkins, A.E.; Kolthammer, J.; Karp, J.S. Performance of Philips Gemini TF PET/CT Scanner with Special Consideration for Its Time-of-Flight Imaging Capabilities. *J. Nucl. Med.* **2007**, *48*, 471–480.
88. Jakoby, B.W.; Bercier, Y.; Watson, C.C.; Bendriem, B.; Townsend, D.W. Performance Characteristics of a New LSO PET/CT Scanner with Extended Axial Field-of-View and PSF Reconstruction. *IEEE Trans. Nucl. Sci.* **2009**, *56*, 633–639. [CrossRef]
89. Valais, I.; David, S.; Michail, C.; Konstantinidis, A.; Kandarakis, I.; Panayiotakis, G.S. Investigation of Luminescent Properties of LSO:Ce, LYSO:Ce and GSO:Ce Crystal Scintillators under Low-Energy γ-Ray Excitation Used in Nuclear Imaging. *Nucl. Instrum. Methods Phys. Res. Sect. Accel. Spectrom. Detect. Assoc. Equip.* **2007**, *581*, 99–102. [CrossRef]
90. Storm, L.; Israel, H.I. Photon Cross Sections from 1 keV to 100 MeV for Elements Z = 1 to Z = 100. *At. Data Nucl. Data Tables* **1970**, *7*, 565–681. [CrossRef]
91. Hubbell, J.H.; Seltzer, S.M. *Tables of X-ray Mass Attenuation Coefficients and Mass Energy-Absorption Coefficients*; NIST Standard Reference Database 126; National Institute of Standards and Technology-PL: Gaithersburg, MD, USA, 1995.
92. Boone, J. X-ray Production, Interaction, and Detection in Diagnostic Imaging. In *Handbook of Medical Imaging. Volume 1: Physics and Psychophysics*; Beutel, J., Kundel, H.L., Van Metter, R.L., Eds.; SPIE Press: Bellingham, WA, USA, 2000; Volume 1, pp. 36–57, ISBN 978-0-8194-7772-9.

Disclaimer/Publisher's Note: The statements, opinions and data contained in all publications are solely those of the individual author(s) and contributor(s) and not of MDPI and/or the editor(s). MDPI and/or the editor(s) disclaim responsibility for any injury to people or property resulting from any ideas, methods, instructions or products referred to in the content.